Simulation-based analysis of micro-robots swimming at the center and near the wall of circular mini-channels

Fatma Zeynep Temel & Serhat Yesilyurt

ONLINE FIRST

A 20975

Microfluidics and Nanofluidics

Springer

Springer

Springer

RESEARCH PAPER

Simulation-based analysis of micro-robots swimming at the center and near the wall of circular mini-channels
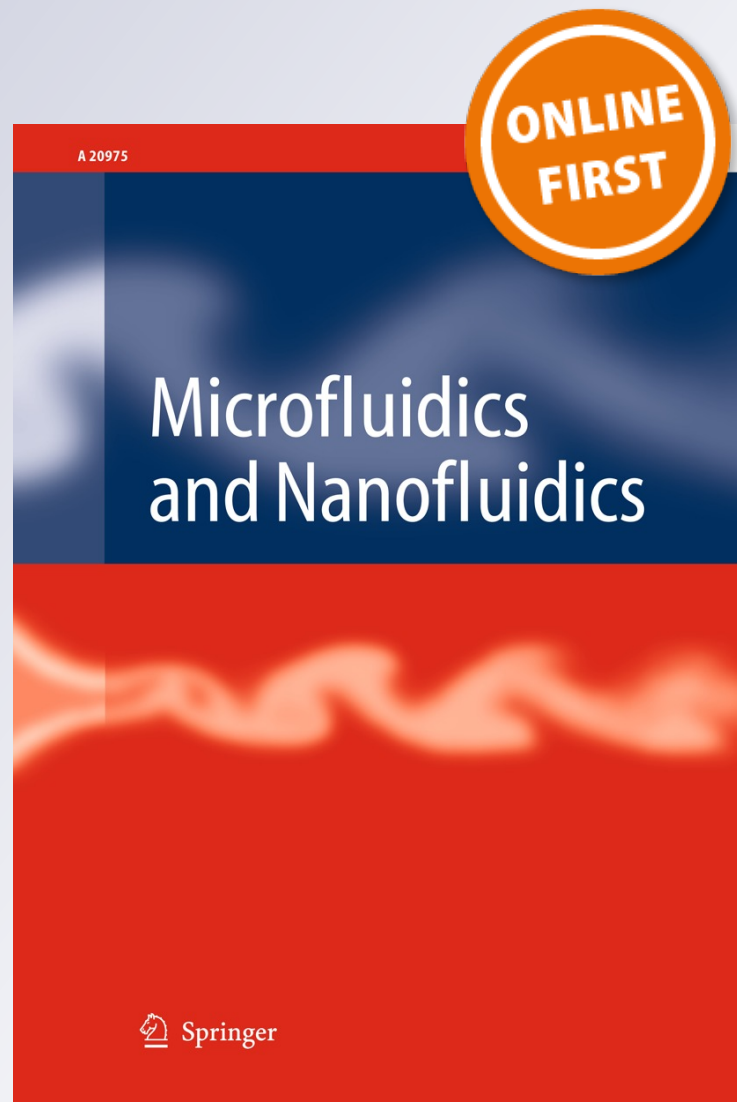
Fatma Zeynep Temel · Serhat Yesilyurt

Abstract Swimming micro-robots have great potential in biomedical applications such as targeted drug delivery, medical diagnosis, and destroying blood clots in arteries. Inspired by swimming microorganisms, micro-robots can move in biofluids with helical tails attached to their bodies. In order to design and navigate micro-robots, hydrodynamic characteristics of the flow field must be understood well. This work presents computational fluid dynamics modeling and analysis of the flow due to the motion of micro-robots that consist of magnetic heads and helical tails inside fluid-filled channels akin to bodily conduits; special emphasis is on the effects of the radial position of the robot. Time-averaged velocities, forces, torques, and efficiency of the micro-robots placed in the channels are analyzed as functions of rotation frequency, helical pitch (wavelength) and helical radius (amplitude) of the tail. Results indicate that robots move faster and more efficiently near the wall than at the center of the channel. Forces acting on micro-robots are asymmetrical due to the chirality of the robot's tail and its motion. Moreover, robots placed near the wall have a different flow pattern around the head when compared to in-center and unbounded swimmers. According to simulation results, time-averaged forward velocity of the robot agrees well with the experimental values measured previously for a robot with almost the same dimensions.

F. Z. Temel · S. Yesilyurt (✉)
Faculty of Engineering and Natural Sciences,
Sabanci University, Orhanli, 34956 Tuzla, Istanbul, Turkey
e-mail: syesilyurt@sabanciuniv.edu

F. Z. Temel
e-mail: zeyneptemel@sabanciuniv.edu

1 Introduction

Bio-inspired swimming micro-robots are attractive tools that can perform variety of medical tasks; a detailed survey is presented by Nelson et al. (2010). For example, millimeter-long robots can be placed inside an artery, navigated through the arterial network to reach a target site, manipulated to perform an operation such as releasing of an anti-clotting agent, and recovered back from the body.

Bacteria such as *Vibrio alginolyticus*, *Escherichia coli* and *Rhodobacter sphaeroides* propel themselves with the rotation of their helical flagella, which are actuated by molecular motors within the body that can rotate as high as at 1 kHz, in the case of *V. algino* (Atsumi et al. 1996; Berg 1993; Armitage and Macnab 1987). The speed of the organism depends on body shape and size, as well as parameters of the flagellar actuation, such as wavelength, frequency, and amplitude (Atsumi et al. 1996; Berg 1993; Armitage and Macnab 1987). Flagellar propulsion mechanisms of microorganisms are adopted successfully by artificial micro-swimmers in recent years (Dreyfus et al. 2005; Zhang et al. 2009; Ghosh and Fischer 2009; Cheang et al. 2010).

Generating and storing power in micro-scales as well as building actuation mechanisms such as molecular motors in nano-scales pose difficulties due to challenges of micro-manufacturing. External magnetic fields compatible with medical procedures was demonstrated successfully for the actuation of swimming micro-robots (Martel et al. 2009). Zhang et al. (2009) manufactured a helical filament from

GaAs with dimensions of 1.8 μm in width, 30 μm in length, and 200 nm in thickness, and attached to a soft magnetic nickel body on one side; authors demonstrated the forward motion of the structure in the direction of the helical axis by applying a rotational magnetic field in that direction and pointed out that linear swimming velocity was affected not only by the size of the magnetic head, but also the strength of the applied magnetic field. Ghosh and Fischer (2009) manufactured and operated chiral colloidal propellers of 200–300 nm width and 1–2 μm length made of silicon dioxide and a thin layer of ferromagnetic material (cobalt) deposited on one side. Those magnetic nanostructured propellers were then navigated in water with micrometer-level precision using rotational magnetic fields.

Hydrodynamic modeling of natural micro-swimmers has been an interest for more than 50 years. Taylor (1951) presented an analysis of the flow induced by small amplitude planar waves propagating on an infinite sheet immersed in a viscous fluid analogous to the propulsion mechanism of spermatozoa. Gray and Hancock (1955) modeled swimming of a sea-urchin spermatozoa based on the fluid forces calculated by the resistive force theory, which offers a general framework for the calculation of the resultant propulsion and drag forces from the integration of local forces in normal and tangential directions that are proportional to the velocity components in those directions over the tail. Lighthill (1975) postulated a line distribution of stokelets on slender bodies and obtained resistive force coefficients for rotating rigid helical tails. Brennen and Winet (1977) presented a broad review of propulsion mechanisms and parameters of microorganisms along with theoretical models. Katz et al. (1975) calculated resistive force coefficients using the slender body theory with distributed stokelets over slender bodies swimming near solid walls. Lauga et al. (2006) modeled circular motion of *E. coli* near solid boundaries using drag coefficients derived by Katz et al. (1975) and validated the model with experimental results (Lauga et al. 2006). Felderhof (2010) showed that confinement in fluid-filled channels significantly affects the speed of an infinitely long swimmer placed at the center of the channel based on a first-order perturbation solution of Stokes equations. Recently, Lauga and Powers (2009) presented a thorough review and a framework for hydrodynamic modeling of swimming organisms including modeling of interactions between bodies and boundaries.

In-channel experiments are significant for their relevance to in vivo applications of micro-robots. Honda et al. (1996) used external actuation by a rotating magnetic field to obtain propagation of a cm-long spiral swimming robot in a silicon-oil-filled, 15-mm-diameter channel. According to their experiments, motion of the robot has a linear relationship with the excitation frequency (Honda et al. 1996). Berke et al. (2008) investigated hydrodynamic interactions of swimming organisms with solid surfaces by measuring the distribution of *E. coli* swimming between glass plates and compared their results with a hydrodynamic model. Giacché et al. (2010) studied bacteria swimming near solid surfaces by using a model based on the boundary element method to predict the near-wall motion of flagellated microorganisms and validated the model with a set of experiments with *E. coli* (Giacché et al. 2010). Recently, we conducted experiments using one-link micro-robots consisting of a permanent magnet $Nd_2Fe_{14}B$ body ($\sim$360 μm in diameter) and a metal helical wire ($\sim$110 μm diameter) attached to the body (Temel and Yesilyurt 2011). One-link robots are rotated inside glycerol-filled glass channels of 1 mm inner-diameter by the rotating magnetic field driven by Helmholtz coil pairs. A proportional relationship between the time-averaged velocity and the rotation frequency is observed up to a step-out frequency, after which robots lose sync with the magnetic field. As the magnetic field strength is increased, higher step-out frequencies are observed similar to the results reported in literature (Ghosh and Fischer 2009; Zhang et al. 2009). The effects of amplitude and wavelength are demonstrated in Erman and Yesilyurt (2011) with autonomous robots placed inside silicon-oil-filled glass channels with the diameter of 3.6 cm.

In vivo applications will benefit from understanding of the flow field induced by the interaction of the micro-robot with the channel wall. This work presents simulation-based analysis of the flow field induced by the one-link swimmer inside a circular channel, hydrodynamic forces and torques acting on the swimmer and the swimming efficiency as a function of the wavelength and amplitude of the helical tail and the radial position of the swimmer. Micro-swimmers are modeled based on the one used in previous experimental work at low Reynolds numbers (Re $\sim 10^{-3}$) (Temel and Yesilyurt 2011). A three-dimensional steady-state computational fluid dynamics (CFD) model is developed and solved with the commercial finite-element software COMSOL Multiphysics (COMSOL AB 2011). Simulations are conducted for two different positions of the swimmer aligned with the channel axis, at the center and near the wall.

2 Methodology

The micro-swimmer modeled here is based on the actual robot used in our experiments which is referred as L2W4 in Temel and Yesilyurt (2011). The swimmer used in the experiments consists of a magnetic head attached to a rigid
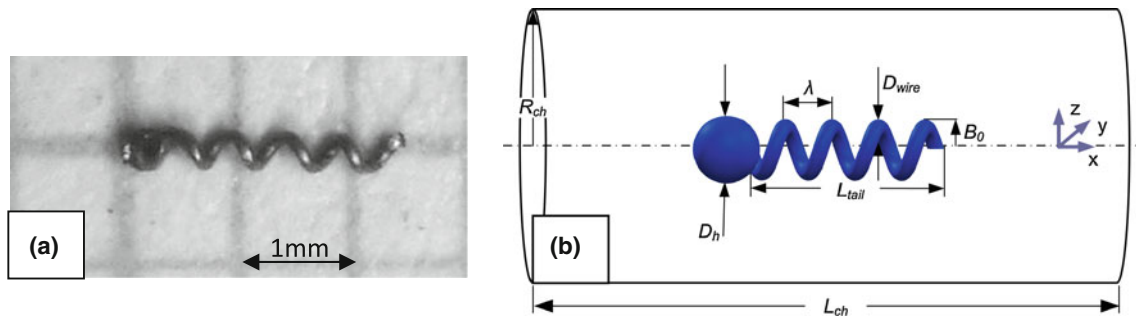
Fig. 1 **a** Micro-robot used in the experiments consists of a magnetic head and a metal right-handed helical tail. **b** Drawing of the micro-robot in CFD model that consists of a spherical head and a left-handed helical tail inside a cylindrical channel

right-handed helical tail with a strong adhesive (Fig. 1a). Nearly spherical lump of $Nd_{12}Fe_{14}B$ magnet is used for the magnetic head, whereas the tail is made of non-magnetic metal wire, which has a thickness of 110 μm and four full waves. Diameter of the magnetic head, length of the helical tail and the amplitude of helical waves are measured as 360 μm, 2.09 mm and 125 μm, respectively. In the CFD model, the magnetic head is assumed to be a perfect sphere and attached to the left-handed helical tail without any gap. The difference between chiralities of the tails makes no difference in the calculated values but only in the directions as confirmed by simulations for robots having the same dimensions but differing only in the chirality of the helices.

The glass channel is filled with glycerol, whose viscosity is $\mu = 0.1$ Pa s, and density is $\rho = 1{,}000$ kg/m^3 in experiments and simulations. Only a 7.2 mm portion of the channel is taken into account in the model as the flow is well within the viscous regime and the motion of the swimmer does not affect the downstream and upstream portions significantly as confirmed by simulations: fluid motion is suppressed within less than a millimeter distance from the swimmer in the flow regime of simulated robots (i.e., for Re $\sim 10^{-3}$) as discussed in Sect. 3.

Geometric dimensions are scaled with the diameter of the head (see Table 1), which is multiplied by the frequency of rotations to set the velocity scale. Thus, Reynolds number used in scaling is the 'frequency Reynolds number':

$$Re_f = \frac{\rho D_h^2 f}{\mu} \tag{1}$$

Table 1 shows actual dimensions and properties of the fluid and corresponding values used in nondimensional equations in the CFD model. In Fig. 1b parameters of the system are shown schematically.

Rotation of the rigid helix, with the unitary frequency in the dimensionless CFD model, is specified as a sinusoidal deformation in **y**- and **z**-directions:

$$\mathbf{d}_{\text{tail}} = \begin{bmatrix} x_{\text{tail}} \\ y_{\text{tail}} \\ z_{\text{tail}} \end{bmatrix} = \begin{bmatrix} x_{\text{tail}} \\ B_0 \cos(\phi - kx_{\text{tail}}) \\ B_0 \sin(\phi - kx_{\text{tail}}) \end{bmatrix} \tag{2}$$

where k is the wave number, B_0 is the amplitude of the helical waves, x_{tail} is the distance from the head and $\phi = \omega t$ is the phase angle that corresponds to the rotation angle of the helix at a given time t and angular frequency ω.

The three-dimensional instantaneous flow around the swimmer inside the channel is modeled with the incompressible Stokes equations for low Reynolds number swimming conditions:

$$0 = -\nabla P + \frac{1}{Re_f} \nabla^2 \mathbf{U}$$
$$\nabla \cdot \mathbf{U} = 0 \tag{3}$$

where P is the pressure, $\mathbf{U} = [u, v, w]'$ is the velocity vector of the fluid and Re_f is the frequency Reynolds number given by (1).

No-slip boundary conditions are imposed on the swimmer and on the channel walls including the inlet and outlet. On the swimmer, velocity is specified by forward motion and rotation of the swimmer having unitary rotational frequency. Namely, we have:

$$\mathbf{U} = 0 \quad \text{at } r = R_{\text{ch}}, \, x = 0 \text{ and } x = L_{\text{ch}} \tag{4}$$

and

$$\mathbf{U} = (\mathbf{e}_x 2\pi) \times \mathbf{p} + [u_{\text{sw}}, 0, 0]' \quad \text{on the swimmer} \tag{5}$$

where r is the radial position, $\mathbf{e}_x$ is the unit vector in the **x**-direction, $\mathbf{p}$ is the position vector on the swimmer surface and u_{sw} is the forward velocity of the swimmer. We only considered the forward motion in the **x**-direction, which is dominant particularly inside the cylindrical channel as also observed in our experiments.

Forward velocity of the swimmer, u_{sw}, is the only variable that needs to be calculated in (5); lateral velocities, which are negligible for in-channel swimming, are set to zero. Angular velocity in the direction of the motion of the micro-robot is specified in simulations, unlike in

Table 1 Geometric parameters of the channel and micro-swimmer

Parameter	Actual value	Dimensionless value
Radius of channel (R_{ch})	0.5 mm	1.39
Length of channel (L_{ch})	7.2 mm	20
Wire diameter of the tail (D_{wire})	0.11 mm	0.306
Length of tail (L_{tail})	2.09 mm	5.81
Diameter of spherical head (D_h)	0.36 mm	1
Density of fluid (ρ)	1,000 kg/m^3	1
Viscosity of fluid (μ)	0.1 Pa s	1/Re

experiments, where finite magnetization of the head and the specified external magnetic field strength lead to a constant magnetic torque, which sets a constraint for the **x**-direction viscous torque for the swimmer.

In order to obtain the forward velocity of the swimmer, the force-free swimming condition is added as a constraint equation:

$$F_x = \int_{S_{sw}} \sigma_{xj} d\mathbf{S}_j = 0, \tag{6}$$

where F_x is the total force on the swimmer in the **x**-direction, σ_{xj} is the stress tensor components in the **x**-direction, $d\mathbf{S}_j = dS\,[n_x, n_y, n_z]'$ is the differential element at the surface that points in the jth direction, S_{sw} is the surface of the swimmer, and n_x, n_y and n_z are surface normal vectors in **x**-, **y**- and **z**-directions.

In (6), where standard summation of repeated indices is implied, the stress tensor in the **x**-direction, σ_{xj}, for incompressible flow is given by:

$$\sigma_{xj} = -P\delta_{xj} + \mu\left(\frac{\partial u}{\partial x_j} + \frac{\partial u_j}{\partial x}\right) \tag{7}$$

where δ_{xj} is the Kronecker's delta, $x_j = \{x, y, z\}$ and $u_j = \{u, v, w\}$.

Commercial finite-element software, COMSOL Multiphysics (COMSOL AB 2011), is used to solve (3) and (6) subject to (4) and (5). The finite-element model consists of 40,000 and 96,000 tetrahedral elements and 225,000 and 530,000 degrees of freedom, for center and near-wall swimming conditions, respectively. The linear system of equations is solved using the PARDISO direct solver.

In CFD simulations, radial position and angular velocity of the swimmer and number and amplitude of helical waves on the tail are varied. Calculated velocities, forces, torques and efficiencies are averaged over full rotations of micro-robots over a set of angular positions, ϕ in (2), that correspond to times at which the snapshot solutions of Stokes equations are obtained.

3 Results

In CFD simulations, frequencies are varied between 1 and 30 Hz, wave amplitudes between 25 and 125 μm, and number of waves between 1 and 5. Radial position of the swimmer is set to zero for swimmers at the center and to 0.3 mm for swimmers near the channel wall. Base-case reference parameter values are set to those for the robot used in experiments, which are $B = 0.125$ mm for the helical radius (wave amplitude) of the tail, $f = 10$ Hz for frequency, and $N_\lambda = 4$ for number of waves on the tail. Only one parameter is varied for each simulation while the others are kept constant. For the swimmer located at the center of the channel, the helical axis lies on the axis of the channel. In order to mimic unbounded swimming conditions, an additional simulation is carried out for comparisons for a swimmer placed inside a channel with radius equals to 3.6 mm (approximately 10 times the diameter of the head) with the base-case parameters.

3.1 Velocity fields

Closed contour surfaces colored gray for positive (backward) and black for negative (forward) velocities are shown in Fig. 2 for swimmers with the base-case values of geometric parameters, (a) in unbounded fluid, (b) in the center of the channel, and (c) near the channel wall. For all cases, the left-handed helical tail of the swimmer rotates in the positive **x**-direction and pushes the fluid in the same direction, while the swimmer moves in the opposite direction. The $u/D_h f$ ratio in Fig. 2 is equal to -0.17 for forward flow (black surface) and 0.17 for backward flow (gray surface), whereas forward velocities of the unbounded, in-center, and near-wall swimmers are -0.67 mm/s ($u/D_h f = -0.186$), -0.7 mm/s ($u/D_h f = -0.195$) and -0.76 mm/s ($u/D_h f = -0.212$), respectively. The black contour surface ($u = -0.61$ mm/s) represents the fluid flow that moves with the swimmer. The gray surface ($u = 0.61$ mm/s) is for the flow in the opposite direction (positive **x**-direction) with respect to the direction of swimming.

Backward flow induced by the rotation of the helical tail and the forward flow due to the motion of the overall swimmer form two distinct surface contours around the tail. Extent of the backward flow for the unbounded swimmer (gray contour surface in Fig. 2a) is only limited to the vicinity of the tail (see Fig. 3) and diminishes immediately behind the tail. Observed flow around the body of the swimmer is due to the motion of the swimmer itself. In Fig. 2b, surface contours are shown for the swimmer placed at the center of the channel; surface contours resemble those around the unbounded swimmer (Fig. 2a). However, there is a weak backward flow

especially around the head of the swimmer in the case of swimming at the center of the channel, which is not shown here but discussed later.

In Fig. 2c, surface contours are shown for the swimmer near the channel wall. Axial velocity contours around the tail remain the same as previous cases for unbounded and center-located swimmers. On the other hand, contours around the head of the near-wall swimmer are distinctly different than the ones observed for unbounded and center swimmers. Based on the similarity between the velocity contours of extreme values around helical tails, we suggest that flow near the tail of the swimmer varies very little with unbounded or in-channel swimming. However, the flow around the head of the near-wall swimmer is significantly different than flows observed for unbounded and center swimmers.

In Fig. 3, axial velocity profiles are demonstrated on segments which are along the **x**-direction, parallel to the axis of the helical tail and tangent to the head of the swimmer at $y = D_h/2$ and $z = 0$ for unbounded and center swimmers and at $y = D_h/2$ and $z = 0.3$ mm for near-wall swimmers. Axial velocities are shown with respect to the axial position relative to the head and at angular positions, $\phi = \{\pi/2, \pi, 3\pi/2, 2\pi\}$, i.e., $t = \{\pi/2\omega, \pi/\omega, 3\pi/2\omega, 2\pi/\omega\}$. At all times, axial velocity profiles are similar for all swimming conditions around the tails of swimmers. However, the axial velocity profile around the head of the near-wall swimmer is significantly different than the profiles for center and unbounded swimmers. Rotation of the helical tail squeezes the fluid between the swimmer and the wall, and forces the flow in both directions. Moreover, close to the head of the near-wall swimmer, there is a clear backward flow in the channel due to the displacement of the fluid by the head. The flow in the channel weakens away from the swimmer and vanishes within a millimeter (diameter of the channel, or the half length of the tail) consistently with the Stokes flow regime. Particularly for the in-channel swimmer, flow vanishes in two distance
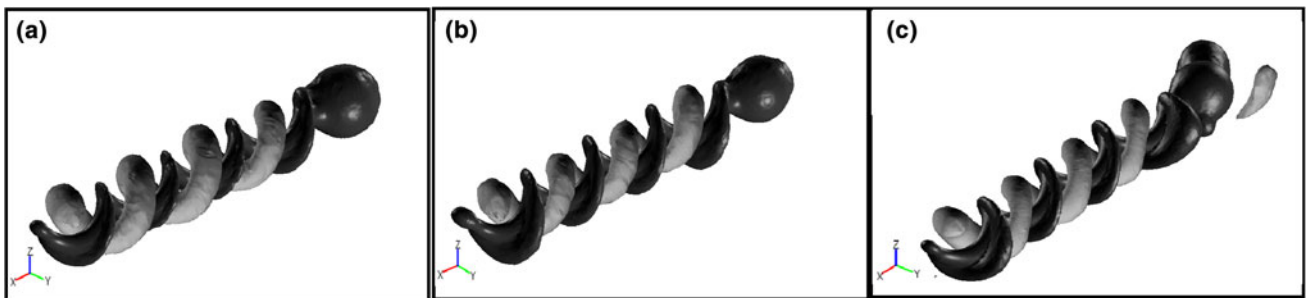

Fig. 2 Closed contour surfaces, which are colored by *gray* for positive (backward—$u/D_h f = 0.17$ and $u = 0.61$ mm/s) and *black* for negative (forward—$u/D_h f = -0.17$ and $u = -0.61$ mm/s) velocities, for swimmers in unbounded fluid (**a**); in the circular channel at the center (**b**); and near the channel wall (**c**); for all cases $\phi = \pi$, i.e., $t = \pi/\omega$. Swimmer is covered with the *black* contour surface, which represents the flow moving with the swimmer

Fig. 3 Axial velocity profile induced by unbounded swimmer (*dashed black lines*) and swimmers inside the channel (*dash-dotted blue lines* for in-center swimmer and *solid red lines* for near-wall swimmer) along the segments parallel to the channel's long axis at $y = D_h/2$ and $z = 0$ for unbounded and center and at $y = D_h/2$ and $z = 0.3$ mm for near-wall swimmers, for angular positions: $\phi = \pi/2$ ($t = \pi/2\omega$) (**a**), $\phi = \pi$ ($t = \pi/\omega$) (**b**), $\phi = 3\pi/2$ ($t = 3\pi/2\omega$) (**c**), $\phi = 2\pi$ ($t = 2\pi/\omega$) (**d**)
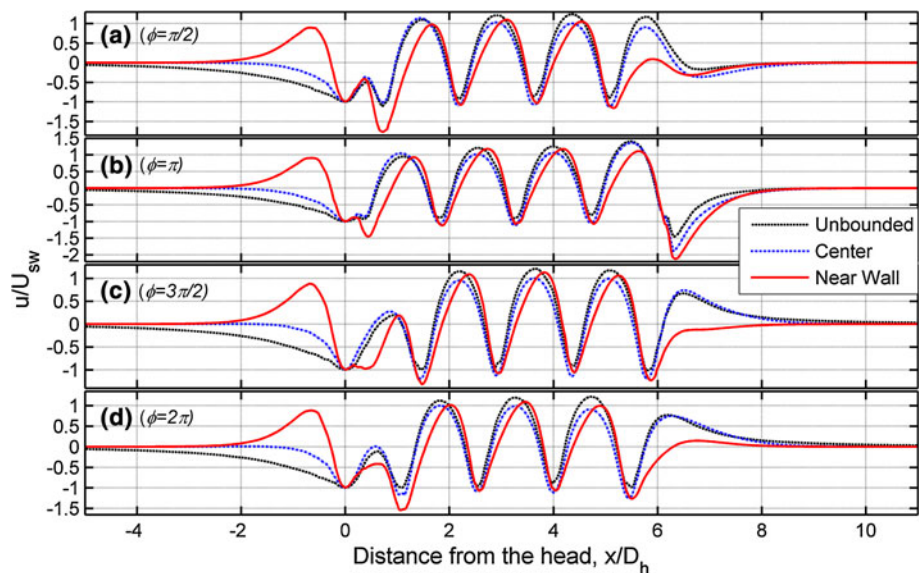
units due to the suppression induced by channel walls. In essence, only the fluid in immediate neighborhood of the swimmer is affected by the motion of the swimmer; the fluid in the rest of the channel remains still.

Distribution of the axial velocity of the flow with respect to the **y**-position at $z = 0$ is shown in Fig. 4 for the swimmer placed along the centerline of the channel for axial positions that correspond to: (a) one-head diameter in front of the swimmer; (b) mid-position of the head; (c) mid-position of the tail; and (d) three head-diameters behind the tail (see the sketches in Fig. 4). In all cases, average axial velocity of the flow in the channel is zero due to the conservation of mass in the close-ended channel. The backward flow of the displaced fluid is clearly observed at all times and axial positions. Despite the symmetry of the spherical head, axial flow is not axisymmetric even in front of the head (Fig. 4a), indicating that the flow around the helical tail has a significant effect on the upstream flow and demonstrating a characteristic feature of the low Reynolds number helical swimming in channels, unlike the swimmer in unbounded fluid for which the flow in front of the swimmer is solely due to the forward motion of the swimmer (not shown here). In Fig. 4b, the flow around the head of the swimmer is due to zero-net flow in the close-ended channel: the forward motion of the swimmer pushes the fluid backward away from the swimmer towards the channel wall. At the mid-section of the tail (Fig. 4c), the axial flow distribution is due to the rotation of the helical tail and alters its direction according to the angular position of the robot. Behind the swimmer away from the

tip of the tail, the axial velocity profile becomes smooth and resembles a simple sine wave with a magnitude reduced by 97.5 % within a millimeter, which is equal to the diameter of the channel (Fig. 4d).

3.2 Swimming speed

Effects of the frequency, amplitude (helical radius), and wavelength (helical pitch) of the helical tail on the swimming speed of the robot were studied for both center and near-wall swimming in circular channels. According to simulation results for base-case parameters ($f = 10$ Hz, $B = 0.125$ μm, and $N_\lambda = 4$), near-wall swimming (1.11 mm/s) is faster than swimming at the center (0.87 mm/s), which is slightly faster than unbounded swimming (0.77 mm/s). Recently, Felderhof (2010) carried out an analytical study based on asymptotic expansions for infinite rotating helices in cylindrical tubes; according to his results, in-channel swimming is always faster than unbounded swimming; for large wave numbers discrepancy is even more significant. However, in previous studies carried out for swimming near planar walls, e.g., by Lauga et al. (2006), the authors concluded that swimming near planar walls reduces the speed of the swimmer for some natural micro-swimmers such as *E. coli*. According to Lauga et al. (2006), a microorganism with a helical tail having three waves reaches the same velocity with a slower rotational speed when the swimmer is placed away from a solid boundary. Discrepancy between the results occur due to the differences of the swimmers studied in Lauga et al.
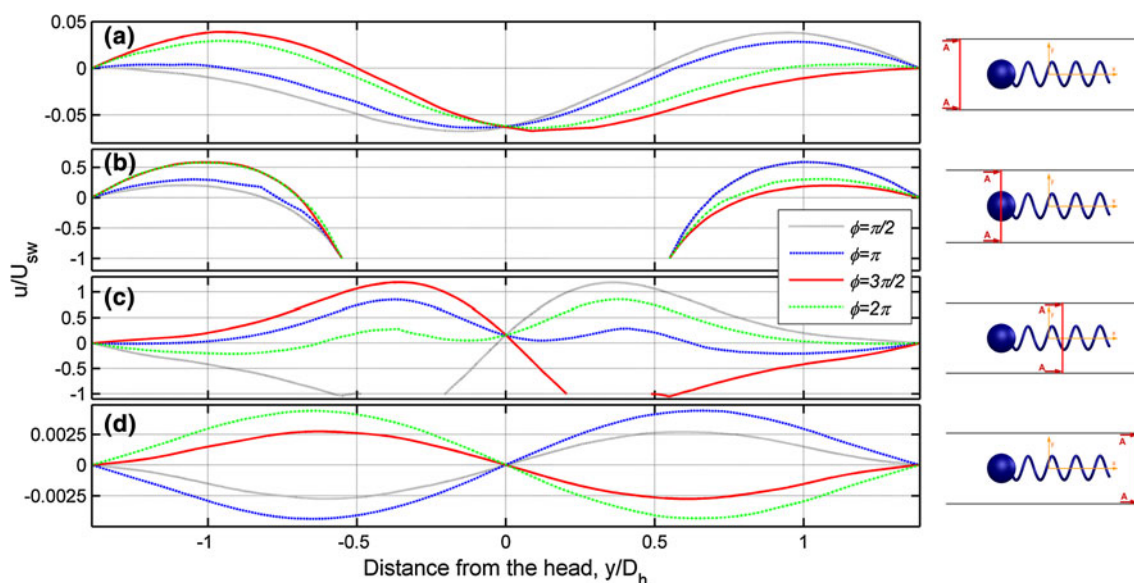

Fig. 4 Axial velocity profile across the channel for axial positions: **a** one-head diameter in front of the swimmer, **b** at the middle of the head, **c** at the middle of the tail, **d** about 1 mm after the tail for $\phi = \pi/2$ ($t = \pi/2\omega$) (*dotted black*), $\phi = \pi$ ($t = \pi/\omega$) (*dashed blue*), $\phi = 3\pi/2$ ($t = 3\pi/2\omega$) (*solid red*), and $\phi = 2\pi$ ($t = 2\pi/\omega$) (*dash-dotted green*)

Fig. 5 Experimental (*solid lines with asterisks*), in-center (*solid lines with circles*) and near-wall (*dashed lines with squares*) swimmer speed of micro-robot having base-case parameters with respect to frequency where $B = 0.125$ μm and $N_\lambda = 4$ (**a**), amplitude where $f = 10$ Hz and $N_\lambda = 4$ (**b**), and number of waves where $f = 10$ Hz and $B = 0.125$ μm (**c**)
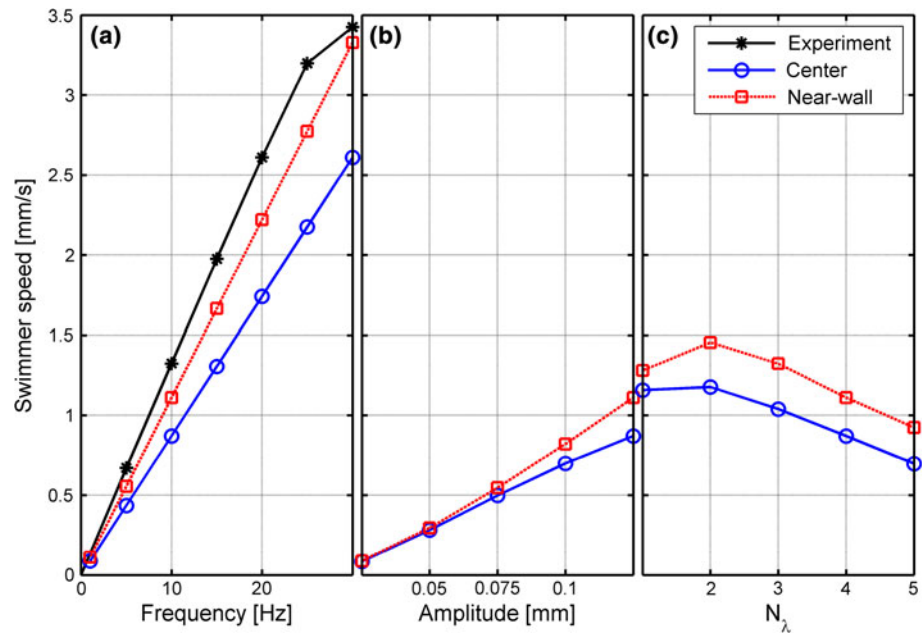
(2006) and in this study: first, the proximity of the organism to the wall is very close in Lauga et al. (2006), about 1 versus 6 % of the radius of the head, here we compare center-swimming versus distance from the wall about 6 % of the radius of the head; second, counter-rotating body and the tail is considered in Lauga et al. (2006) and the one-link swimmer with the glued body and tail considered here. The distance between the robot and solid wall has an utmost effect; as robots get closer to the channel wall, they tend slow down and even come to the full-stop when they are in full contact (Temel, dissertation in progress). Moreover, for spherical objects in circular channels, Happel and Brenner (1983) show that there is an optimal radial position where the drag force over the sphere is minimum; as the sphere gets further closer to the wall the drag force raises sharply.

The forward velocity of the micro-swimmer is investigated in Fig. 5 with respect to rotational frequency, wave amplitude and number of waves. The effect of the frequency on the swimmer's speed is shown in Fig. 5a. Swimming speed increases linearly with the frequency for both radial positions, similar to the relationship between the speed and frequency for the infinite helix in an unbounded medium as calculated analytically (Taylor 1951; Lighthill 1975), and observed by experiments (Temel and Yesilyurt 2011; Zhang et al. 2009; Ghosh and Fischer 2009). According to simulations, swimming speed is about 0.145 times the wave propagation speed on the tail for near-wall swimming and for all frequencies; similarly center-swimming speed is 0.134 times the wave propagation speed. Speeds observed in experiments are slightly faster than those we obtained in simulations. In the experiments, which are conducted with horizontal tubes,

the radial position of the swimmer was not measured, but it was clear that gravity causes swimmer to remain very close to the wall at all times.

Figure 5b shows the change in swimming speed with respect to the amplitude of helical waves. According to the analytical results for free swimmers (Lighthill 1975; Higdon 1979), swimming speed increases quadratically with the amplitude. In addition, Felderhof (2010) concludes that based on his asymptotic solution, infinite helices in circular channels swim proportional to the square of the amplitude. According to the simulation results for near-wall swimmer, swimming speed is proportional to the amplitude with a power >1. The difference between simulation results and aforementioned analytical results is expected due to the effect of the finite amplitude of the helix; quadratic behavior reported in approximate analytical studies is valid for small amplitudes near zero. Furthermore, for micro-swimmers moving at the center of the cylindrical channel, swimming speed does not increase quadratically, but it shows a slight decrease in the rate of increase of the swimming speed as the wave amplitude increases.

Number of waves affects the speed of the swimmer similarly for both center and near-wall swimming (Fig. 5c). According to simulation results, swimming speed reaches its maximum value when $N_\lambda = 2$, and decreases linearly for higher N_λ values. According to analytical studies, there is an optimal value of the number of waves that maximizes the swimming speed for swimmers with helical tails in unbounded fluid (Lighthill 1975; Higdon 1979). For the same rotational speed, based on an analysis using stokelets, Higdon (1979) showed that the maximum swimming speed is reached when the number of waves is 3

Fig. 6 x-Force acting on the head normalized by the theoretical spherical drag ($3\pi\mu D_h U$) with respect to dimensionless time for unbounded (*dash-dotted line*), in-center (*dashed line*), and near-wall (*solid line*) swimmers
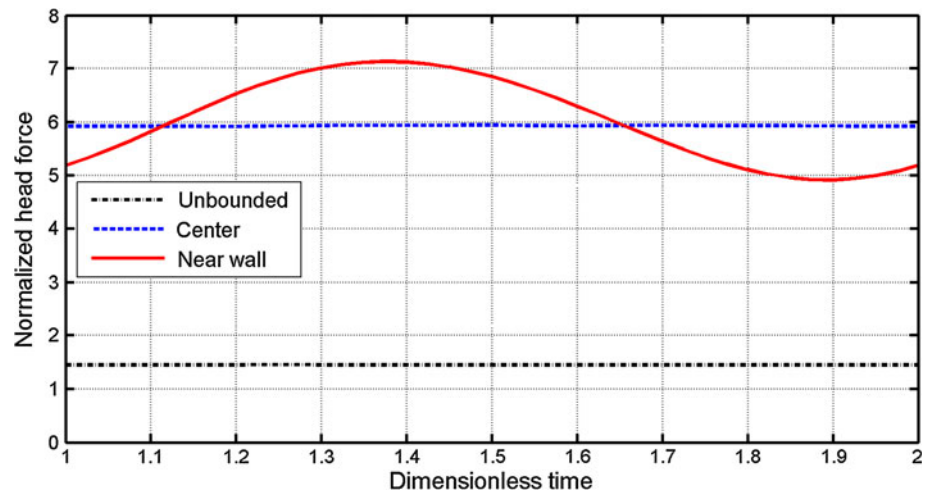
for a swimmer with L/A ratio being 10 and a/A ratio being 0.02, where L is the length of the flagellum, A is the radius of the body, and a is the radius of the flagellum and that the point of the maximum velocity depends on the geometry of the swimmer. Higdon (1979) also stated that, the decrease in the swimming velocity after the optimal point is a result of the decrease in efficiency due to the disappearance of the slenderness of helical structures as wavelength decreases. For swimming of infinite helices in circular tubes, Felderhof (2010) also concludes that in-channel swimming has an optimal value of the wave number depending on the physical parameters of the swimmer and the environment.

3.3 Forces and torques on the swimmer

The net force in the **x**-direction is zero due to free-swimming condition given by (6), and the net torque in the **x**-direction equals to the external torque (e.g., magnetic). For swimmers with base-case parameters, net torque values in the **x**-direction are calculated as 0.4 nN-m for unbounded swimming, 0.487 nN-m for swimming at the center of the circular channel, and 0.535 nN-m for swimming near the wall. Clearly, the **x**-torque is the lowest for unbounded swimming and the highest for near-wall swimming, latter due to the traction forces between the swimmer and the cylindrical channel walls.

For the swimmer at the center of the circular channel, **y**- and **z**-forces have zero means with respect to time and have a phase shift in time due to rotation of the helical tail (not shown here). For the swimmer near the channel wall, net forces in the **y**- and **z**-directions are negative and positive, respectively. The negative **y**-force indicates that the swimmer with the left-handed helical tail is pushed to its left side (port) during its forward motion. Non-zero **y**-force is clearly due to the traction force from the rotation of the swimmer near the wall. On the other hand, according to simulation results, a small positive force in the

z-direction indicates that the swimmer is pushed away from the wall, and there may be a stable position for the swimmer near the wall, similar to the 'trapping' of bacteria near walls (Lauga et al. 2006; Shum et al. 2010). According to simulation results, normal-stress distribution around the swimmer as a whole contributes to the **z**-force against the wall; individual contributions from the head and tail are comparable. Furthermore, in our ongoing computational studies, it is observed that the radial force increases for higher forward speeds when the motion is in the opposite direction as compared to the rotation (such as left-handed helices rotating in the positive direction or vice versa) (Temel, dissertation in progress).

In Fig. 6, normalized drag force on the spherical head of the swimmer is plotted against time. Drag force on the spherical head is normalized by the theoretical drag force, $3\pi\mu D_h U$, on a sphere of diameter D_h, moving with velocity U in an unbounded fluid with viscosity μ. Averaged values over 12 different angular positions are obtained as 1.445 for unbounded, 5.928 for center, and 6.04 for near-wall swimming for base-case parameters. The difference between averaged values for swimmers inside the channel is very little. However, the difference between the unbounded swimmer and in-channel swimmers is more than fourfold. Moreover, the head drag for the unbounded swimmer is nearly 45 % larger than the theoretical drag for an isolated sphere; this increase is mostly due to the difference between flow fields for an isolated sphere and one with the helical tail. Lastly, results show that the drag force on the spherical head has the largest fluctuations due to variations of the axial velocity near the head for near-wall swimming (see Fig. 3).

In Fig. 7, variations of time-averaged forces are plotted with respect to frequency (Fig. 7a), amplitude (Fig. 7b) and number of waves on the tail (Fig. 7c) for near-wall swimming. Time-averaged forces on the swimmer in **y**- and **z**-directions and on the spherical head in the

Fig. 7 Time-averaged **y**- and **z**-forces for near-wall swimmers (*solid lines with circles and squares*) with respect to frequency (**a**), amplitude (**b**) and number of waves (**c**) in comparison to drag force on the head (*solid lines with asterisks*); schematic representation of forces acting on the robot swimming near the wall (**d**)
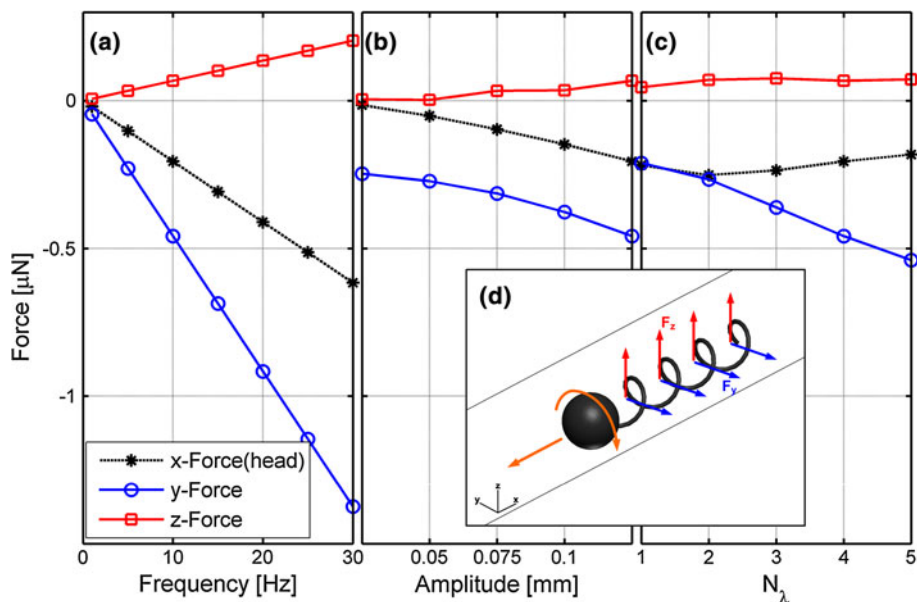
x-direction increase linearly with the frequency (Fig. 7a), with a constant factor multiplying the head-force in the **x**-direction: about 2.23 for the **y**-force and 0.33 for the **z**-force. The ratio of the **y**- and **z**-forces is also constant, about 6.76, with respect to the frequency. Figure 7b illustrates that the **y**-force on the swimmer remains significant due to the traction induced by the rotation even though the **x**-force on the head and **z**-force on the swimmer tends to zero as the amplitude goes to zero. The magnitude of the **x**-force on the head and **y**- and **z**-forces on the whole swimmer increase with the wave amplitude (Fig. 7b).

As for the dependence on the number of waves, the **y**-force increases with the increasing number of waves on the tail but the **z**-force tends to saturate (Fig. 7c). The increase in the **y**-force with respect to both the amplitude and the number of waves is consistent with increasing traction force due to the rotation. However, the **x**-force on the head decreases as the number of waves increases (Fig. 7c) due the decreasing swimmer speed (see also Fig. 5c).

Torques on swimmers in all directions are computed from the integration of the cross-product of the position vector with respect to the center of mass of each swimmer and the stress tensor at the swimmer's surface for near-wall swimming. The position of the center of mass is calculated for each robot according to the geometry of the helical tail that varies with the amplitude and wavelength. For robots with small tail mass (small amplitude and large wavelength), swimmer's center of mass is closer to the head than for robots with large tail mass (large amplitude and small wavelength).

Magnitudes of the torques in **x**- and **z**-directions increase linearly with the frequency (Fig. 8a). The **x**-torque, which is the direction of rotation, is the largest; the **z**-torque on the swimmer due to uneven traction between the head and tail of the swimmer is next in size (about 1.4 % of the **x**-torque); whereas **y**-torque is observed as zero. This result is somewhat consistent with the parallel-positioning of the microorganisms swimming near flat surfaces as observed by Lauga et al. (2006). As the amplitude increases, **x**-torque increases as well due to increasing resistance to rotation, the **y**-torque remains almost zero and **z**-torque decreases and even changes its direction from positive to negative (Fig. 8b). For small amplitudes, the positive **z**-torque indicates that the traction force from the spherical head overcomes the traction force from the tail with respect to the center of mass of the swimmer which is closer to the head, hence the positive **z**-torque is observed. On the other hand, the traction from the tail is larger than the traction from the head for larger amplitudes and leads to the negative **z**-torque that forces the swimmer to turn clockwise with respect to the **z**-axis as observed in the experiments.

The **x**-torque remains almost constant as the number of waves increased to 2 from 1 (Fig. 8c), and increases at a higher rate for larger number of waves than 2. For small wave numbers the **x**-torque on the head is dominant and the effect from the tail is indiscernible. As the wave number increases, the **x**-torque on the tail becomes important.

The **z**-torque decreases with the increasing number of waves similarly to the behavior with respect to the amplitude. With the increasing number of waves on the helical tail, the traction force from the tail increases and dominates the one from the head and the **z**-torque changes its direction

Fig. 8 Time-averaged torques in **y**- and **z**-directions for near-wall swimmers (*solid lines with circles and squares*) with respect to rotational frequency (**a**), wave amplitude (**b**) and number of waves on the helical tail (**c**) in comparison to the **x**-torque (*dashed lines with asterisks*); schematic representation of torques on the base-case robot swimming near the wall (**d**); *top-view* of the micro-robot in experiments (**e**) (actual robot has a right-handed helical tail, mirror-image is shown here)
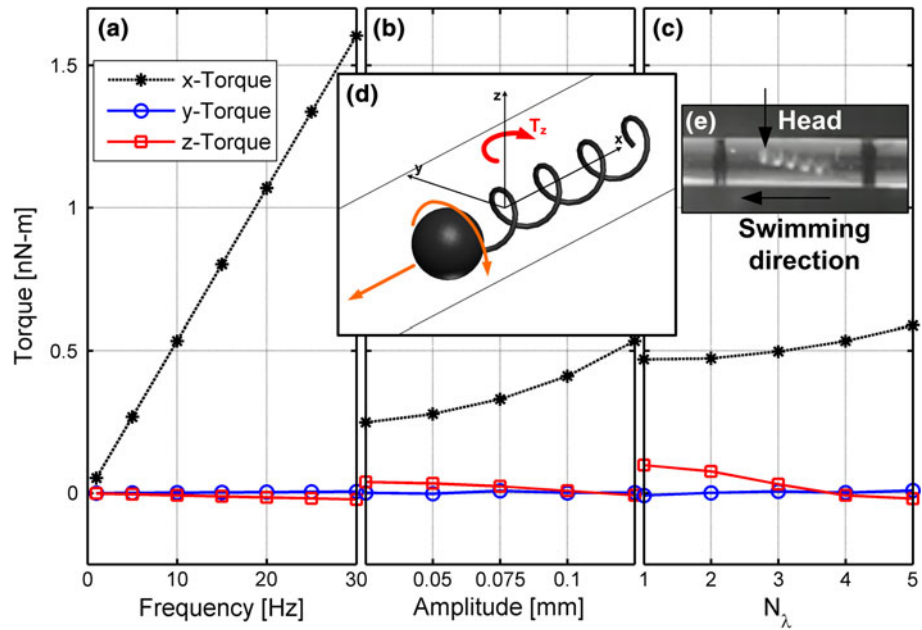
(Fig. 8c). The non-zero **z**-torque causes the robot to change its alignment with the channel's axis; counter-clockwise when the number of waves is smaller than 4, and clockwise for N_λ equals 4 and 5. Thus, it is likely for the swimmer to follow a path, which is not parallel to channel's long axis, as observed in our experiments (Fig. 8e).

3.4 Efficiency

Efficiency of low Reynolds number swimmers with flagellar propulsion is defined as the ratio of rates of work to linearly push the swimmer and to rotate the tail (Purcell 1976). The net torque due to swimmer's rotational motion is well-defined and can be computed accurately. Nevertheless, since the net force on the swimmer in the direction of its motion is zero, an approximate definition of the efficiency is necessary. For swimmers with spherical heads, some authors typically use the ratio of the drag on the body to the total dissipation in the fluid (Lighthill 1975; Higdon 1979). However, this approach neglects the tail resistance and is less meaningful for swimmers with relatively small heads compared to their tails. In (6), total force in the axial direction is calculated and set to zero in order to satisfy the free-swimming condition and to obtain the axial velocity; in essence, the total drag of the swimmer is balanced by the propulsion force. Therefore, an alternative figure of merit is defined for the efficiency based on the net propulsion force in the swimming direction and calculated from the integration of the product of the stress tensor in the same direction and the Heaviside function that masks the stress. Then the efficiency is determined from:

$$\eta = \frac{|u| \int_S \sigma_{xj} H(\sigma_{xj}) dS_j}{2\pi f |T_x|} \quad (8)$$

Here, u is the linear velocity in the swimming direction, here **x**-direction, f is the rotation frequency, T_x is the rotational torque in the axial direction, $H(.)$ is the Heaviside step function that masks the stress tensor component in the swimming direction on the swimmer, i.e., $H(x) = x$ for $x > 0$ and $H(x) = 0$ for $x < 0$.

Efficiency values for in-center and near-wall swimming robots are shown in Fig. 9. Efficiency stays constant as the frequency increases because of the linear relationship between the time-averaged **x**-direction velocity and the rotational frequency for both positions of the robot. The near-wall swimming is more effective (~ 1.5 %) compared to in-center swimming of the micro-robot (~ 1.21 %) and the simulations show that free swimmer is slightly less efficient (~ 1.2 %) than the in-channel swimmer. Efficiency values are on the order of 1 %, as also stated by Purcell for helical swimmers in low Reynolds number flow regimes (Purcell 1976).

Change in the efficiency with respect to wave amplitude is presented in Fig. 9b. Similar to the velocity, efficiency is proportional to the wave amplitude with the power >1 for near-wall swimming micro-robot. As the wave amplitude increases, efficiency increases for both near-wall and in-center swimmers, yet the near-wall swimming is slightly more efficient than swimming at the center of the channel.

Increase in number of waves results in decrease in efficiency (Fig. 9c). As the number of waves increases, friction over the tail also increases and since the velocity decreases, overall the efficiency of the robot decreases with

Fig. 9 Frequency (**a**), wave amplitude (**b**) and number of waves (**c**) dependence of efficiency for in-center (*solid lines with circles*) and near wall (*solid lines with squares*) swimming micro-robots
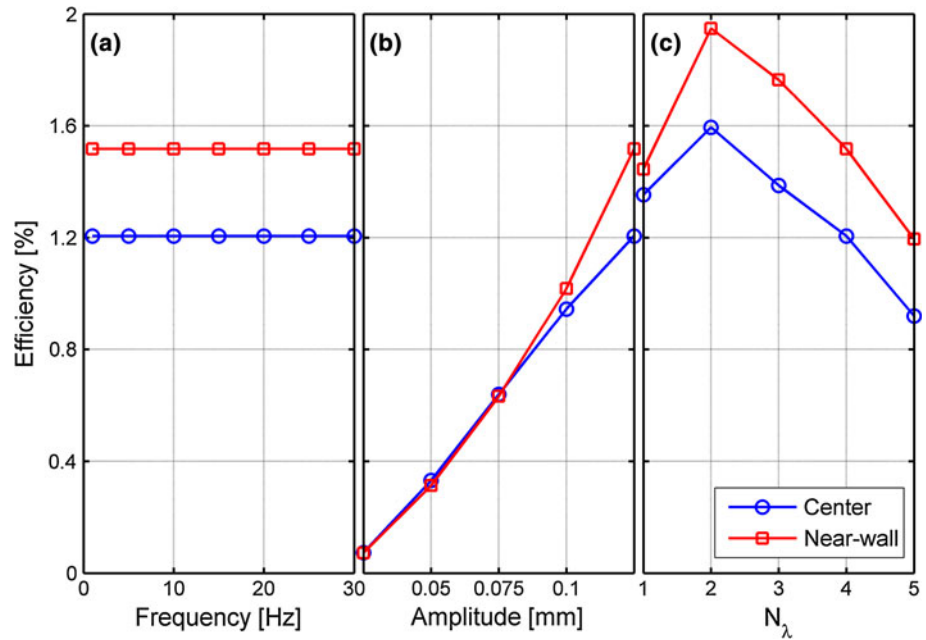
the number of waves. However, we obtain the optimum value for $N_\lambda = 2$ similar to what is observed for the velocity of the swimmer.

4 Conclusion

Simulation results are presented for swimming micro-robots with helical tails and traveling in circular tubes and compared with experimental results for a robot with approximately the same dimensions. Simulations are performed for two different radial positions of the robot in the channel: at the center and near the wall. The effects of frequency, wave amplitude, and number of waves on the forward velocity, forces on **y**- and **z**-directions, torques along **x**-, **y**- and **z**-axis and efficiency are studied for both radial positions.

Forward and backward flows induced by the tail's rotation and the motion of the swimmer form a bidirectional flow field around the helical tail and diminish within a short distance away from the swimmer. The axial velocity profile around the helical tail for unbounded, in-center and near-wall swimming cases are similar. However, due to the rotation of the helical tail, the squeezed fluid between channel boundaries and the swimmer is forced to move in opposite directions near the head. Forward velocity of the swimmer near the wall is larger than the one swimming at the center, which is also slightly faster than the unbounded swimmer agreeing well with the results presented by Felderhof (2010). A linear relationship between the frequency and the time-averaged forward velocity of the swimmer is observed in simulations, which agree well with

experiments for frequencies less than the step-out frequency for which the magnetic torque cannot overcome the rotational drag in experiments.

Forces acting on the swimmer in **y**- and **z**- directions vary significantly between the swimmers placed at the center and near the wall. For the swimmer placed along the axis of the channel at the center, **y**- and **z**-direction forces are nearly zero, unlike for the swimmer placed near the wall. Negative tangential force due to traction force shows that the swimmer is pushed sideways during its forward motion. For the swimmer near the wall, the **y**-torque is almost zero and the **z**-torque depends on the tail geometry, which also alters the position of the center of mass. A small positive **z**-torque for the swimmer used in experiments indicates that the swimmer has a tendency to travel with an angle with respect to the axis of the channel which is also observed in experiments. An appropriate metric for the efficiency of the micro-swimmer is proposed based on the propulsion force, and results show that near-wall swimmers are more efficient than swimmers at the center; efficiencies are on the order of 1 %, which is expected for low Reynolds number swimmers.

Design and control of micro-robots for in vivo medical applications can benefit greatly from the results and detailed analysis presented here. It is shown that the radial position of a micro-robot swimming inside a circular channel has a major effect on the swimming velocity and the efficiency of the robot. Furthermore, detailed analysis of the forces and torques acting on the swimmer shows that the stable radial position and the orientation of the swimmer depend strongly on the geometries of the tail and the head.

References

Armitage JP, Macnab RM (1987) Unidirectional, intermittent rotation of the flagellum of *Rhodobacter sphaeroides*. J Bacteriol 169(2):514–518

Atsumi T, Maekawa Y, Yamada T, Kawagishi I, Imae Y, Homma M (1996) Effect of viscosity on swimming by the lateral and polar flagella of *Vibrio alginolyticus*. J Bacteriol 178(16):5024–5026

Berg HC (1993) Random walks in biology. Princeton University Press, Princeton

Berke AP, Turner L, Berg HC, Lauga E (2008) Hydrodynamic attraction of swimming microorganisms by surfaces. Phys Rev Lett 101:038102

Brennen C, Winet H (1977) Fluid mechanics of propulsion by cilia and flagella. Annu Rev Fluid Mech 9:339–398

Cheang UK, Toy D, Lee JH, Kim MJ (2010) Fabrication and magnetic control of bacteria-inspired robotic microswimmers. Appl Phys Lett 97:213704

COMSOL-AB (2011) Comsol multiphysics modelling guide. COM-SOL, Stockholm

Dreyfus R, Baudry J, Roper ML, Fermigier M, Stone HA, Bibette J (2005) Microscopic artificial swimmers. Nature 437(6):862–864

Erman AG, Yesilyurt S (2011) Swimming of onboard-powered autonomous robots in viscous fluid filled channels. IEEE international conference on mechatronics ICM 2011. Istanbul

Felderhof BU (2010) Swimming at low Reynolds number of a cylindrical body in a circular tube. Phys Fluids 22:1136041–1136046

Ghosh A, Fischer P (2009) Controlled propulsion of artificial magnetic nanostructured propellers. Nano Lett 9(6):2243–2245

Giacché D, Ishikawa T, Yamaguchi T (2010) Hydrodynamic entrapment of bacteria swimming near a solid surface. Phys Rev E 82:056309

Gray J, Hancock G (1955) The propulsion of sea-urchin spermatozoa. J Exp Biol 32:802–814

Happel J, Brenner H (1983) Low Reynolds number hydrodynamics with special applications to particulate media. The Hague and Boston and Hingham, MA

Higdon JJ (1979) The hydrodynamics of flagellar propulsion: helical waves. J Fluid Mech 94(2):331–351

Honda T, Arai KI, Ishiyama K (1996) Micro swimming mechanisms propelled by external magnetic fields. IEEE Trans Magn 32(5):5085–5087

Katz DF, Blake JR, Paveri-Fontana SL (1975) On the movement of slender bodies near plane boundaries at low Reynolds number. J Fluid Mech 72:529–540

Lauga E, Powers TR (2009) The hydrodynamics of swimming microorganisms. Rep Prog Phys 72:1–36

Lauga E, DiLuzio WR, Whitesides GM, Stone HA (2006) Swimming in circles: motion of bacteria near solid boundaries. Biophys J 90:400–412

Lighthill SJ (1975) Mathematical biofluid dynamics. Society for Industrial and Applied Mathematics, Philadelphia

Martel S, Felfoul O, Mathieu J-B, Chanu A, Tamaz S, Mohammadi M, Mankiewicz M, Tabatabaei N (2009) MRI-based medical nanorobotic platform for the control of magnetic nanoparticles and flagellated bacteria for target interventions in human capillaries. Int J Robotics Res 28:1169–1182

Nelson BJ, Kaliakatsos IK, Abbott JJ (2010) Microrobots for minimally invasive medicine. Annu Rev Biomed Eng 12:55–85

Purcell EM (1976) Life at low Reynolds number. Am J Phys 45(1):3–11

Shum H, Gaffney EA, Smith DJ (2010) Modeling bacterial behaviour close to no-slip plane boundary: the influence of bacterial geometry. Proc R Soc A 466:1725–1748

Taylor SG (1951) Analysis of the swimming of microscopic organisms. Proc R Soc Lond 209(A):447–461

Temel FZ, Yesilyurt S (2011). Magnetically actuated micro swimming of bio-inspired robots in mini channels. IEEE international conference on mechatronics, ICM2011. Istanbul

Zhang L, Abbott JJ, Dong L, Peyer K, Kratochvil BE, Zhang H et al (2009) Characterization of the swimming properties of artificial bacterial flagella. Nano Lett 9(10):3663–3667